Topological nodal line semimetal in an orthorhombic graphene network structure

Jian-Tao Wang, Changfeng Chen, and Yoshiyuki Kawazoe

Phys. Rev. B **97**, 245147 — Published 28 June 2018

DOI: 10.1103/PhysRevB.97.245147

Topological nodal line semimetal in an orthorhombic graphene network structure

Jian-Tao Wang,[1,2,*] Changfeng Chen,[3] and Yoshiyuki Kawazoe[4,5]

[1]*Beijing National Laboratory for Condensed Matter Physics, Institute of Physics, Chinese Academy of Sciences, Beijing 100190, China*
[2]*School of Physics, University of Chinese Academy of Sciences, Beijing 100049, China*
[3] *Department of Physics and High Pressure Science and Engineering Center, University of Nevada, Las Vegas, Nevada 89154, USA*
[4]*New Industry Creation Hatchery Center, Tohoku University, Sendai 980-8579, Japan*
[5]*Department of Physics and Nanotechnology, SRM Institute of Science and Technology, Kattankulathur 603203, Tamil Nadu, India*

(Dated: May 22, 2018)

Topological semimetals are a fascinating class of quantum materials that possess extraordinary electronic and transport properties. These materials have attracted great interest in recent years for their fundamental significance and potential device applications. Currently a major focus in this research field is to theoretically explore and predict and experimentally verify and realize material systems that exhibit a rich variety of topological semimetallic behavior, which would allow a comprehensive characterization of the intriguing properties and a full understanding of the underlying mechanisms. In this work, we report on *ab initio* calculations that identify a carbon allotrope with the simple orthorhombic crystal structure in *Pbcm* (D_{2h}^{11}) symmetry. This carbon allotrope can be constructed by inserting zigzag carbon chains between the graphene layers in graphite or by a crystalline modification of (3,3) carbon nanotube with a double cell reconstruction mechanism. Its dynamical stability has been conformed by phonon and molecular dynamics simulations. Electronic band calculations indicate that it is a nodal line semimetal comprising two nodal lines that go through the whole Brillouin zone in bulk and a projected surface flat band around the Fermi level. The present findings establish an additional topological semimetal system in the nanostructured carbon allotropes family and offer insights into its outstanding structural and electronic properties.

I. INTRODUCTION

Carbon is capable of forming an extremely rich variety of structural allotropes due to the versatile hybridized bonding states of its $2s^22p^2$ valence electrons [1–5]. At ambient conditions, graphite is the most stable carbon phase; its honeycomb lattice can be viewed as a planar molecule comprising benzene rings in an all-sp^2 bonding state, which hosts a semimetallic electronic structure [6]. At high pressures, graphite can be converted into insulating cubic or hexagonal diamond at high temperatures [7–11] or diamond-like cold-compressed graphite phases at room temperature [12–19], such as M-carbon [14], bct-C_4 [15], and W-carbon [16] in all-sp^3 bonding. Modern advances in synthesis techniques have made it possible to convert graphitic carbon sheets into new structural forms, such as zero-dimensional fullerenes [20], one-dimensional nanotubes [21], two-dimensional (2D) graphene [22], and three-dimensional (3D) polybenzene [23, 24] in all-sp^2 bonding. The well-known monolayer 2D graphene has a Dirac point in its 2D Brillouin zone (BZ), characterized as a nodal-point semimetal [25]. Recent theoretical studies suggested that 3D graphene networks support topological semimetals harboring continuous nodal lines that go through the whole BZ or nodal rings that reside inside a mirror plane of the BZ [26–36]. Topological semimetals with node rings have been found in all-sp^2 carbon network structures such as Mackay-Terrones carbon crystal [26], body-centered orthorhombic C_{16} (bco-C_{16}) [29], and a body-centered tetragonal C_{16} (bct-C_{16}) [33]. Meanwhile topological semimetals with node lines have been found in sp^2-sp^3 hybrid network structures such as interpenetrated graphene network C_6 (ign-C_6) [27], body-centered tetragonal C_{12} (bct-C_{12}) [28], and body-centered tetragonal C_{40} (bct-C_{40}) [34]. Moreover, 3D conductive interconnected graphene networks have been synthesized by chemical vapor deposition [37]. These advances open exciting avenues for constructing additional graphene framework structures.

In this paper, we report on a computational discovery of a carbon allotrope with the simple orthorhombic crystal structure in *Pbcm* (D_{2h}^{11}) symmetry, which can be constructed by inserting zigzag carbon chains between the graphene layers in graphite or by a crystalline modification of (3,3) carbon nanotube (CNT) with a double cell reconstruction mechanism. The resulting interpenetrated graphene network structure contains 12-atoms in its unit cell, thus termed so-C_{12}. Total-energy calculations show that so-C_{12} is more stable than the polymeric (3,3) CNT and comparable to the recently reported ign-C_6 [27] and bct-C_{12} [28] network structures. Its dynamical stability has been verified by phonon mode analysis and molecular dynamics simulations. Electronic band structure calculations show that so-C_{12} contains two mirror symmetric nodal lines in the bulk and one projected surface flat band around the Fermi level on its (010) sur-

*e-mail address:wjt@aphy.iphy.ac.cn

face. These findings place so-C_{12} as an additional member among topological node-line semimetals [38–52], and the results of the present work is expected to help further understand and characterize these fascinating materials.

II. COMPUTATIONAL METHOD

Our calculations were carried out using the density functional theory as implemented in the Vienna *ab initio* simulation package (VASP) [53]. The generalized gradient approximation (GGA) developed by Armiento-Mattsson (AM05) [54] were adopted for the exchange-correlation function for the structural relaxation. The all-electron projector augmented wave (PAW) method [55] was adopted with $2s^2 2p^2$ treated as valence electrons. A plane-wave basis set with a large energy cutoff of 800 eV was used. Convergence criteria employed for both the electronic self-consistent relaxation and the ionic relaxation were set to 10^{-8} eV and 0.01 eV/Å for energy and force, respectively. The bulk and surface electronic band structures are calculated using the standard GGA-PBE method [56], while the band gaps are corrected using a hybrid density functional based on the Heyd-Scuseria-Ernzerhof scheme (HSE06) [57]. Phonon calculations were performed using the phonopy code [58]. The so-C_{12} carbon structure is predicted in a double cell reconstruction pathway of (3,3) CNT based on a multi-stage phase transformation simulation method [59].

III. RESULTS AND DISCUSSION

We present in Fig. 1(a) the orthorhombic graphene network structure of so-C_{12}, which can be constructed by inserting zigzag carbon chains between the graphene layers in AA stacking along the x direction or AB stacking along the y direction. The calculated equilibrium lattice parameters are $a = 4.313$ Å, $b = 8.604$ Å, and $c = 2.461$ Å, occupying the $4d_1$ (0.0507, 0.2104, 0.25), $4d_2$ (0.0763, 0.0351, 0.25), and $4d_3$ (0.5783, 0.5052, 0.25) Wyckoff positions denoted by C_1, C_2 and C_3, respectively. The carbon atoms on the $4d_1$ and $4d_3$ sites form four zigzag carbon chains with aromatic sp^2 hybridization, while the carbon atoms on the $4d_2$ sites form two zigzag carbon chains with diamond-like sp^3 hybridization. Thus, there are three sets of distinct carbon-carbon bonds in this structure, namely two sp^3 single longer bonds of 1.512 Å (C_2-C_3 and C_2-C_1) and 1.520 Å (C_2-C_2), and a shorter sp^2 aromatic bond of 1.406 Å (C_1-C_1 and C_3-C_3). There are also two sets of distinct bond angles: 108.04^o for $\angle C_2$-C_2-C_2, 111.38^o for $\angle C_2$-C_2-C_1, and 111.04^o for $\angle C_2$-C_2-C_3, which are on average close to the 109.5^o angle in diamond; 118.95^o for $\angle C_2$-C_3-C_3, 118.90^o for $\angle C_2$-C_1-C_1, and 122.05^o for $\angle C_3$-C_3-C_3, which are on average close to the 120^o angle in graphene.

It is noted that so-C_{12} can be produced by a crystalline modification of (3,3) CNT. At the initial stage, the small

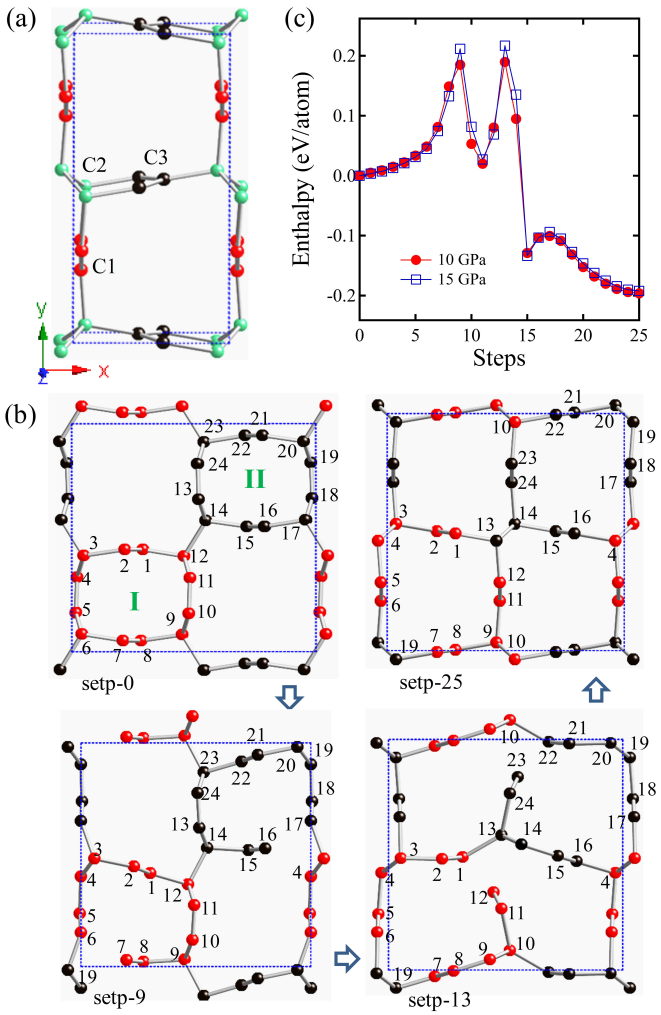

FIG. 1: The crystal structure of so-C_{12} in $Pbcm$ (D_{2h}^{11}) symmetry. (a) The 12-atom unit cell of so-C_{12} with lattice parameters $a = 4.313$ Å, $b = 8.604$ Å, and $c = 2.461$ Å, occupying the $4d_1$ (0.0507, 0.2104, 0.25), $4d_2$ (0.0763, 0.0351, 0.25), and $4d_3$ (0.5783, 0.5052, 0.25) Wyckoff positions denoted by C_1, C_2 and C_3, respectively. (b) A double cell reconstruction pathway from polymeric (3,3) CNT toward so-C_{12} with bond breaking between atoms 6-7 and 16-17 at step-9 and between atoms 1-12 and 22-23 at step-13. The atoms are marked as red in tube-I and black in tube-II, respectively. The initial stage pathway from (3,3) CNT toward polymeric (3,3) CNT is shown in Fig. S1 in Supplemental Material [62]. (c) Enthalpy versus pathway from polymeric (3,3) CNT toward so-C_{12} at 10 and 15 GPa.

(3,3) CNT can spontaneously turn into polymeric (3,3) CNT [60, 61] under pressure (see Fig. S1 in Supplemental Material [62]). A double cell reconstruction pathway from polymeric (3,3) CNT toward so-C_{12} is showed in Fig. 1(b) and the enthalpy versus pathway is plotted in Fig. 1(c) at 10 and 15 GPa. There are two sharp enthalpy peaks in Fig. 1(c). The first peak corresponds to the bond breaking between atoms 6-7 and 16-17 at step-9, followed by the enthalpy decrease with the rebonding

TABLE I: Calculated equilibrium structural parameters (space group, volume V_0, lattice parameters a, b, and c, bond lengths d_{C-C}), total energy E_{tot}, bulk modulus B_0, and electronic band gap E_g for diamond, polymeric CNT-(3,3), bco-C_{16}, bct-C_{12}, ign-C_6, so-C_{12} and graphite, compared to available experimental data for diamond and graphite [7].

Structure	Method	V_0 (Å^3/atom)	a (Å)	b (Å)	c (Å)	d_{C-C} (Å)	E_{tot} (eV)	B_0 (GPa)	E_g (eV)
Diamond ($Fd\bar{3}m$)	AM05	5.60	3.552			1.538	-9.018	451	5.36
	Exp[7]	5.67	3.567			1.544		446	5.47
CNT-(3,3) ($Imma$)	AM05	7.98	8.536	2.485	9.025	1.338∼1.566	-8.703	304	0.32
bco-C_{16} ($Imma$)	AM05	7.70	7.806	4.877	3.237	1.382∼1.459	-8.671	315	semimetal
bct-C_{12} ($I4/mcm$)	AM05	7.66	8.645	8.645	2.460	1.406∼1.517	-8.838	320	semimetal
ign-C_6 ($Cmcm$)	AM05	7.60	5.899	6.281	2.459	1.406∼1.522	-8.852	323	semimetal
so-C_{12} ($Pbcm$)	AM05	7.61	4.313	8.604	2.461	1.406∼1.520	-8.851	322	semimetal
Graphite ($P6_3/mmc$)	AM05	8.81	2.462		6.710	1.422	-9.045	280	semimetal
	Exp[7]	8.78	2.460		6.704	1.420		286	

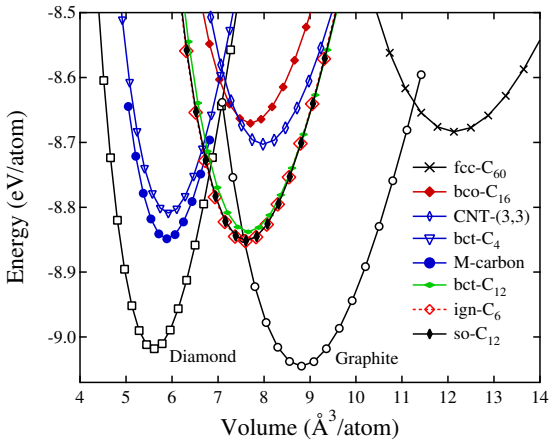

FIG. 2: Calculated energy *versus* volume per atom for so-C_{12} compared to graphite, diamond, fcc-C_{60} [63], bco-C_{16} [29], bct-C_4 [15], M-carbon [14], bct-C_{12} [28], ign-C_6 [27] and polymeric (3,3) CNT [61].

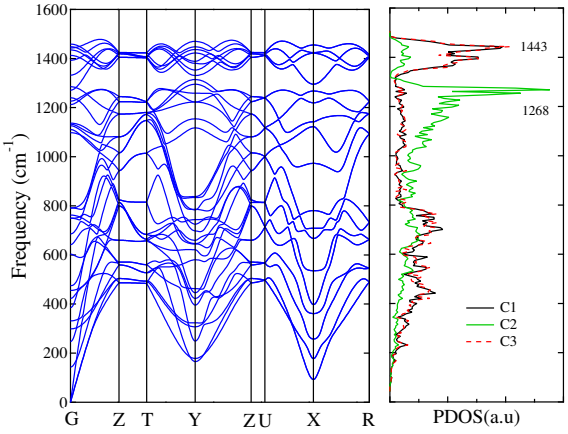

FIG. 3: Phonon band structures and partial density of states (PDOS) for so-C_{12}. The peaks around 1443 cm^{-1} and 1268 cm^{-1} are related to sp^2 and sp^3 bonding, respectively.

between atoms 7-19 and 16-4 around step-11; the second peak corresponds to the bond breaking between atoms 1-12 and 22-23 at step-13, followed by the rebonding with atoms 13 and 10 with the bond rotation of atoms 13-14 and 9-10, respectively, to form the final so-C_{12} structure. Throughout this *bond rotation assisted* two stage reconstruction pathway, the enthalpy barriers are estimated to be 0.19−0.22 eV [see Fig. 1(c)], which is similar to the findings in cold-compressed graphite phase transformations [16].

Figure 2 shows the total energy per atom as a function of volume for so-C_{12} compared with the results for diamond, graphite, fcc-C_{60} [63], ign-C_6 [27], bct-C_{12} [28], bco-C_{16} [29], bct-C_4 [15], M-carbon [14], and polymeric (3,3) CNT [61]. The results show that so-C_{12} is slightly (0.16∼0.19 eV per atom) higher in energy than diamond and graphite, while it is comparably stable as ign-C_6, bct-C_{12}, bct-C_4 and M-carbon, and more stable than bco-C_{16}, fcc-C_{60}, and polymeric (3,3) CNT. By fitting the calculated total energy as a function of volume to Murnaghan's equation of state [64], we obtained the bulk modulus of 322 GPa for so-C_{12}, which is close to the results for bct-C_{12} and ign-C_6 (see Table I) due to their similar atomic density and bonding nature.

For comparison, possible pathways from polymeric (3,3) CNT toward bct-C_{12} and ign-C_6 are also simulated at 10 GPa (see Fig. S2 in Supplemental Material [62]). Along the pathway toward bct-C_{12}, there are four bond breakings between atoms 6-7, 1-12, 16-17 and 22-23 at step-11, resulting in an enthalpy barrier of 0.30 eV; meanwhile, along the pathway toward ign-C_6, the CNTs are squashed firstly with the tube rotation and then the squashed CNT-2 inserts into CNT-1 at step 12, resulting in an enthalpy barrier of 0.34 eV. These enthalpy barriers are larger than the values of 0.19−0.22 eV for the pathway toward so-C_{12}. Thus so-C_{12} is energetically more favorable compared to bct-C_{12} and ign-C_6 in terms of the kinetics in the reconstruction pathway.

Since energetic calculations alone cannot establish the

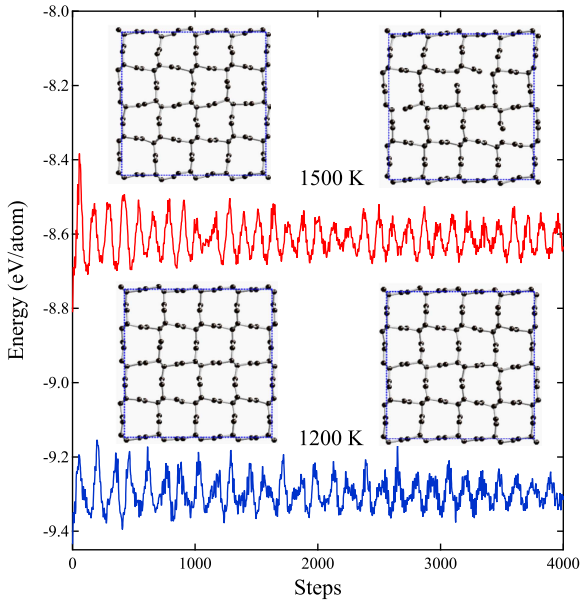

FIG. 4: Energy fluctuations of so-C_{12} in AIMD simulations at 1200 K and1500 K. Insets depict the structural changes at step 1000 and 4000 during the simulations.

stability of a crystal structure, a thorough analysis of the dynamic and thermal stability is required. To assess the dynamical stability, we have calculated phonon dispersion and partial density of states (PDOS), and the obtained results are shown in Fig. 3. It is seen that there are two main peaks around 1443 cm^{-1} and 1268 cm^{-1} in the PDOS. The peak around 1443 cm^{-1} is related to the C_1 and C_3 carbon atoms in sp^2 bonding similar to the finding in all-sp^2 bco-C_{16} [29], while the peak around 1268 cm^{-1} is related to the C_2 carbon atoms in sp^3 bonding similar to the finding in diamond [65]. There are also some peaks below 800 cm^{-1} related to the C_1, C_2, and C_3 carbon atoms in sp^2-sp^3 hybrid bonds. No imaginary frequency exists in the entire BZ and PDOS, confirming the dynamical stability of so-C_{12}. To examine the thermal stability, we have performed *ab initio* molecular dynamics (AIMD) simulations with the canonical (NVT) ensemble by the Nosé thermostat [66] with a step of 1 fs. The systems are modeled by a 4×2×1 supercell. The energy fluctuations at 1200 and 1500 K are presented in Fig. 4. The structures around step 1000 and 4000 are given in the insets of Fig. 4. It is seen that after heating up to 1200 K for 4 ps, no structural changes occur. With temperature increasing up to 1500 K, the structure becomes unstable with some bond breaking between the C_1-C_2 and C_2-C_3 bonds. These results indicate that so-C_{12}, once synthesized, can sustain high temperatures up to 1200 K.

Finally we discuss the electronic properties of so-C_{12}. Fig. 5(a) shows the calculated bulk band structure at equilibrium lattice parameters. It is seen that the valence and conduction bands exhibit linear dispersion near the

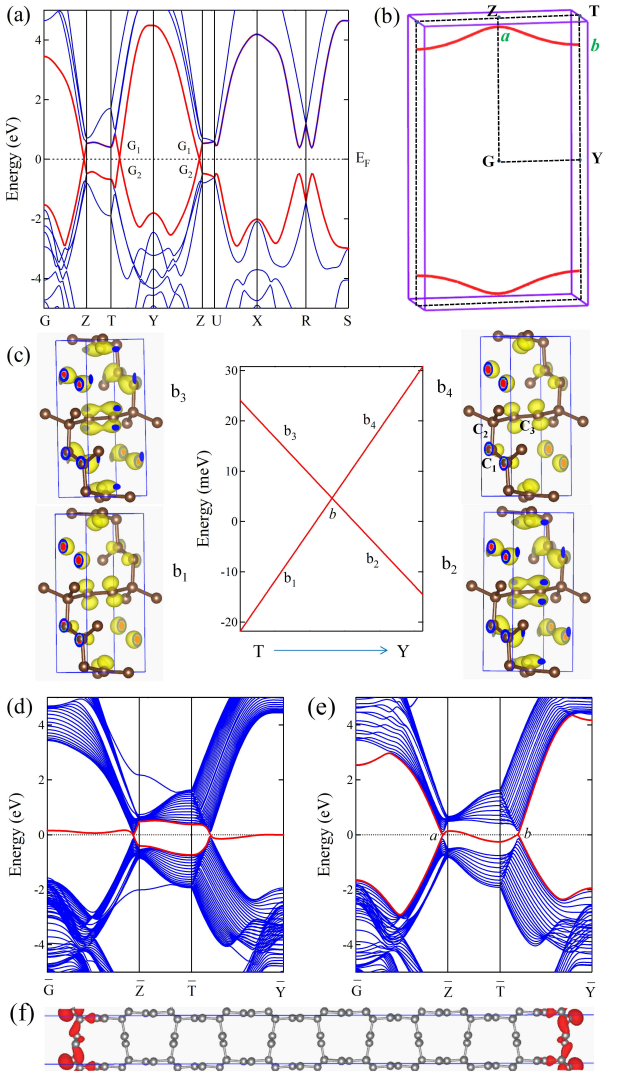

FIG. 5: Calculated bulk and surface band structures of so-C_{12} at equilibrium lattice parameters. (a) The bulk band structure along several high-symmetry directions. G_1 and G_2 indicate the irreducible representations of the two crossing bands, respectively. (b) The Brillouin zone (BZ) with several high-symmetry momenta indicated, and the nodal lines (red), formed by the band crossing points, in the G-Z-T-Y mirror plane. The *a* and *b* points represent the nodal point located along G-Z and T-Y line, respectively. (c) The band-decomposed charge density isosurfaces (0.07 $e/Å^3$) around the nodal point *b* along T-Y direction in BZ. (d,e) The (010) surface states obtained using a ten-layer-thick slab geometry along the [010] direction. The surface flat band (red line) can be inside or outside the surface projected nodal lines, depending on the termination of the surface without (d) or with (e) saturation by hydrogen atoms. The projected surface BZ $\bar{G}$-$\bar{Z}$-$\bar{T}$-$\bar{Y}$ is marked relative to G-Z-T-Y in bulk in (b). (f) Partial charge density isosurfaces (0.05 $e/Å^3$) related to the (red) surface bands in (d) at the $\bar{G}$ point. The outermost atoms are C_2 and C_3 with dangling bonds on C_2 sites.

Fermi energy and cross at the Fermi level (E_F) to form several nodal points along the high symmetric directions

of G-Z, T-Y, and Y-Z in the bulk BZ. Further analysis of the band structure in the full BZ indicates that the band crossing points (or nodal points) of the valence and conduction bands in so-C_{12} form two discrete *saddle* nodal lines inside a mirror plane G-Z-T-Y [see Fig. 5(b)] with an inversion symmetry about the center of G in the bulk BZ. The states near the crossing points around the nodal lines are formed by the inversion of the valence and conduction bands. To clarify this point, we have calculated the band decomposed charge density near the nodal point b on the high symmetric direction T-Y in BZ [see Fig. 5(c)]. One can see that the charge around the nodal points near the Fermi level are located on the C_1 and C_3 atoms and show the π-band character related to the p orbitals. The charge distributions for b_1 (and b_4) are 53.3% from C_1-p_x and 45.1% from C_3-p_y, while for b_2 (and b_3) the values are 49.3% from C_1-p_x and 49.3% from C_3-p_y orbitals. The obvious difference between the charge distributions of $b_1(b_4)$ and $b_2(b_3)$ reveal that the inversion of the valence and conduction bands on both the left and right side of the nodal point. This band inversion can be described by two crossing π bands of G_1 and G_2 throughout the full BZ around the nodal lines. Furthermore, these node lines are protected by the coexistence of time reversal (T) and spatial inversion (P) symmetry [26]. It is also noted that the spin-orbit coupling may open up a gap at the band crossing points, but the extremely weak (0.13∼0.74 meV) coupling strength in carbon [26, 29, 30] is not expected to alter the semimetallic state at room temperature.

Figure 5(d,e) show the surface band structures calculated using a ten-layer thick slab geometry along the [010] crystalline direction [see Fig. 5(f)]. The surface dangling bonds in Fig. 5(e) are saturated with hydrogen atoms. The projected surface BZ $\bar{G}$-$\bar{Z}$-$\bar{T}$-$\bar{Y}$ is marked corresponding to G-Z-T-Y in bulk as shown in Fig. 5(b). It is seen that when the resulted nodal lines are projected onto the surface BZ, they can produce one topologically protected surface flat band around the Fermi level, either outside [region containing the BZ boundaries in Fig. 4(e)] or inside [region containing the $\bar{G}$ point in Fig. 5(d)] of two symmetric (up and down) nodal lines, depending on the termination of the surface with or without saturation by hydrogen atoms. In the Fig. 5(f) the partial charge density isosurfaces related to the energy bands around the Fermi level in Fig. 5(d) at $\bar{G}$ point are plotted. The electronic charges are located on the top most surface carbon layers, confirming that the surface flat band is indeed deriving from the surface atoms. Beside the surface with the outermost atoms of C_2 and C_3 used in Fig. 5(d,e), there is another truncated surface with the outermost atoms of C_1. The calculated surface band structures show similar surface states as plotted in Fig. S3 in the Supplemental Material [62]. These surface states predicted for the nodal line semimetals should be detectable by photoelectron spectroscopy and be compared to ARPES experimental data [50].

As a topological nodal line semimetal, the nodal line structure is usually protected by the topological invariant, *i.e.* the Berry phase (a $\mathbb{Z}_2$-type invariant) along a closed path encircling the nodal line [67]. To clarify this point, we have calculated the Berry phase using the Wannier Tools package [68] based on a Wannier tight-binding model constructed by Wannier90 [69]. The Berry phase with a closed loop surrounding the nodal lines (see Fig. S4(c) in the Supplemental Material [62]) is calculated to be π. Further, the Berry phase along the line passing through the BZ parallel to the k_y axis is calculated. If the line is inside the area between two separated nodal lines (see Fig. S4(b) in the Supplemental Material [62]), the result is either 0 or π. The nonzero quantized Berry phase further confirms the nodal-line feature in so-C_{12} carbon. The appearance of surface states at the surface of nodal line semimetal arises from a quantized Berry phase. Since the Berry phase is equal to π for any closed path that interlinks with the nodal line, the surface states should connect the a and b points on the projected nodal loop in the 2D momentum space in Figs. 5(d,e) since the surface states and the nodal line in bulk are at the same energy level.

According to the classification of topological nodal line semimetals recently suggested by Hyart *et al.* [67], topological semimetals in 3D graphene networks can be divided into two types: type-A has closed nodal rings that reside inside a mirror plane of the BZ, while type-B has continuous nodal lines that go through the whole BZ. The type-A nodal line semimetals have been found in all-sp^2 carbon network structures such as bco-C_{16} [29] and bct-C_{16} [33]. The so-C_{12} reported in this work has a type-B nodal line in sp^2-sp^3 hybrid network like that in ign-C_6 [27] and mC16 [36]. When the nodal line is projected onto certain surfaces to form a drumhead-like surface flat bands either inside or outside of the nodal lines [29]. Meanwhile, bct-C_{40} [34] is a nodal net semimetal consisting of type-B nodal lines in sp^2-sp^3 hybrid network structure and has two coupled drumhead-like flat bands around the Fermi level on its surface. Beside these nodal line or nodal net semimetals, the 3D Weyl-surface semimetals are also reported in triangular graphene network TGN(2,2) [35], quadrilateral graphene network QGN(2,2) [35], and hexagonal graphene network HGN(2,2) [35]. It should be noted such Weyl surfaces are closely related to an additional sublattice-symmetry operator in the tight-binding model [35], in contrast to the nodal nets reported in bct-C_{40} [34]. A similar Dirac surface was also reported in the higher-symmetry bct-C_{12} [28], but it should decay into type-B nodal lines in the lower-symmetry so-C_{12} phase reported here.

IV. CONCLUSION

In conclusion, we have identified by *ab initio* calculations a simple orthorhombic carbon allotrope in *Pbcm* (D_{2h}^{11}) symmetry. This so-C_{12} carbon phase can be characterized as an interconnected graphene network struc-

ture contains 12-atoms in its unit cell and possibly synthesized by inserting zigzag carbon chains between the graphene layers in graphite or by a crystalline modification of (3,3) carbon nanotube with a double cell reconstructing mechanism. Electronic band structure calculations reveal that so-C_{12} belongs to a B-type topological nodal line semimetals and possesses two periodically continuous lines in momentum space. Moreover, when the nodal lines in bulk are projected onto the surface BZ, they produce one topologically protected surface flat band around the Fermi level, either outside or inside of two symmetric nodal lines, depending on the termination of the surface with or without saturation by hydrogen atoms. The present results establish an additional nanostructured carbon phase that is expected to contribute to further characterization of structural and electronic properties and a full understanding of the underlying mechanisms in a large class of topological semimetals.

ACKNOWLEDGMENTS

The authors thank Dr. Hongming Weng for valuable discussions and help on the Berry phase calculation. This study was supported by the National Natural Science Foundation of China (Grants No. 11674364) and the Strategic Priority Research Program of the Chinese Academy of Sciences (Grant No. XDB07000000). C. F. C. acknowledges support by DOE under Cooperative Agreement No. DE-NA0001982.

[1] E. A. Belenkov and V. A. Greshnyakov, Phys. Solid State **55,** 1754 (2013).
[2] R. H. Baughman, H. Eckhardt, and M. Kertesz, J. Chem. Phys. **87,** 6687 (1987).
[3] J. T. Wang, C. F. Chen, H. D. Li, H. Mizuseki, and Y. Kawazoe, Sci. Rep. **6,** 24665 (2016); DOI: 10.1038/srep24665.
[4] A. San-Miguel and P. Toulemonde, High Press. Res. **25,** 159 (2005).
[5] J. T. Wang, C. F. Chen, H. Mizuseki, and Y. Kawazoe, Phys. Chem. Chem. Phys. DOI:10.1039/c7cp08380g (2018).
[6] G. P. Mikitik and Yu V. Sharlai, Phys. Rev. B **73**, 235112 (2006).
[7] F. Occelli, P. Loubeyre, and R. Letoullec, Nat. Mater. **2,** 151 (2003).
[8] R. Clarke and C. Uher, Adv. Phys. **33,** 469 (1984).
[9] I. Irifune, A. Kurio, S. Sakamoto, T. Inoue, and H. Sumiya, Nature **421,** 599 (2003).
[10] S. Scandolo, M. Bernasconi, G. L. Chiarotti, P. Focher, and E. Tosatti, Phys. Rev. Lett. **74,** 4015 (1995).
[11] P. Németh, L. A. J. Garvie, T. Aoki, N. Dubrovinskaia, L. Dubrovinsky, and P. B. Buseck, Nat. Commun. **5,** 5447 (2014).
[12] W. L. Mao, H. K. Mao, P. J. Eng, T. P. Trainor, M. Newville, C. C. Kao, D. L. Heinz, J. Shu, Y. Meng, and R. J. Hemley, Science **302,** 425 (2003).
[13] H. Y. Niu, X. Q. Chen, S. B. Wang, D. Z. Li, W. L. Mao, and Y. Y. Li, Phys. Rev. Lett. **108,** 135501 (2012).
[14] Q. Li, Y. M. Ma, A. R.Oganov, H. B. Wang, H. Wang, Y. Xu, T. Cui, H. K. Mao, and G. T. Zou, Phys. Rev. Lett. **102,** 175506 (2009).
[15] K. Umemoto, R. M. Wentzcovitch, S. Saito, and T. Miyake, Phys. Rev. Lett. **104,** 125504 (2010).
[16] J. T. Wang, C. F. Chen, and Y. Kawazoe, Phys. Rev. Lett. **106,** 075501 (2011).
[17] J. T. Wang, C. F. Chen, and Y. Kawazoe J. Chem. Phys. **137,** 024502 (2012).
[18] M. Amsler, J.A. Flores-Livas, L. Lehtovaara, F. Balima, S.A. Ghasemi, D. Machon, S. Pailhes, A. Willand, D. Caliste, S. Botti, A. San Miguel, S. Goedecker, and M. A. L. Marques, Phys. Rev. Lett. **108,** 065501 (2012).
[19] Z. S. Zhao, F. Tian, X. Dong, Q. Li, Q. Q. Wang, H. Wang, X. Zhong, B. Xu, D. L. Yu, J. L. He, H. T. Wang, Y. M. Ma, and Y. J. Tian, J. Am. Chem. Soc. **134,** 12362 (2012).
[20] H. W. Kroto, J. R. Heath, S. C. Obrien, R. F. Curl, and R. E. Smaliey, Nature **318,** 162 (1985).
[21] S. Iijima, Nature **354,** 56 (1991).
[22] K. S. Novoselov, A. K. Geim, S. V. Morozov, D. Jiang, Y. Zhang, S. V. Dubonos, I. V. Grigorieva, and A. A. Firsov, Science **306**, 666 (2004).
[23] J. T. Wang, C. F. Chen, E. G. Wang, and Y. Kawazoe, Sci. Rep. **4,** 4339 (2014); dio:10.1038/srep04339.
[24] H. A. Calderon, I. Estrada-Guel, F. Alvarez-Ramirez, V. G. Hadjiev, and F. C. Robles-Hernandez, Carbon, **102,** 288 (2016).
[25] M. Z. Hasan and C. L. Kane, Rev. Mod. Phys. **82,** 3045 (2010).
[26] H. Weng, Y. Liang, Q. Xu, R. Yu, Z. Fang, X. Dai, and Y. Kawazoe, Phys. Rev. B **92**, 045108 (2015).
[27] Y. P. Chen, Y. E. Xie, S. A. Yang, H. Pan, F. Zhang, M. L. Cohen, and S. B. Zhang, Nano Lett. **15,** 6974 (2015).
[28] X. Dong, M. Hu, J. L. He, Y. J. Tian, and H. T. Wang, Sci. Rep. **5,** 10713 (2015); doi: 10.1038/srep10713.
[29] J. T. Wang, H. Weng, S. Nie, Z. Fang, Y. Kawazoe, C. F. Chen, Phys. Rev. Lett. **116,** 195501 (2016).
[30] Y. Cheng, J. Du, R. Melnik, Y. Kawazoe, and B. Wen, Carbon **98,** 468 (2016).
[31] B. Yang, H. C. Zhou, X. M. Zhang, X. B. Liu, and M. W. Zhao, Carbon **113,** 40 (2017).
[32] C. Y. Zhong, Y. P. Chen, Z. M. Yu, Y. Xie, H. Wang, S. A. Yang, and S. B. Zhang, Nat. Commun. **8,** 15641 (2017).
[33] Y. Cheng, X. Feng, X. T. Cao, B. Wen, Q. Wang, Y. Kawazoe, and P. Jena, Small 2017, 1602894 (2017); DOI:10.1002/smll.201602894.
[34] J. T. Wang, S. M. Nie, H. Weng, Y. Kawazoe, and C. F. Chen, Phys. Rev. Lett. **120,** 026402 (2018).
[35] C. Y. Zhong, Y. P. Chen, Y. Xie, S. A. Yang, Marvin L. Cohenc, and S. B. Zhang, Nanoscale **8,** 7232 (2016).
[36] X. Feng, Q. S. Wu, Y. Cheng, B. Wen, Q. Wang, Y. Kawazoe, and P. Jena, Carbon **127,** 527 (2018).
[37] Z. Chen, W. Ren, L. Gao, B. Liu, S. Pei, and H. Cheng,

Nat. Mater. **10,** 424 (2011).
[38] A. A. Burkov, M. D. Hook, and L. Balents, Phys. Rev. B **84,** 235126 (2011).
[39] M. Phillips and V. Aji, Phys. Rev. B **90,** 115111 (2014).
[40] C. Fang, Y. Chen, H. Y. Kee, and L. Fu, Phys. Rev. B **92,** 081201 (2015).
[41] Y. Kim, B. J. Wieder, C. L. Kane, and A. M. Rappe, Phys. Rev. Lett. **115**, 036806 (2015).
[42] R. Yu, H. Weng, Z. Fang, X. Dai, and X. Hu, Phys. Rev. Lett. **115**, 036807 (2015).
[43] T. T. Heikkila and G. E. Volovik, New J. Phys. **17,** 093019 (2015).
[44] K. Mullen, B. Uchoa, and D. T. Glatzhofer, Phys. Rev. Lett. **115,** 026403 (2015).
[45] L. S. Xie, L. M. Schoop, E. M. Seibel, Q. D. Gibson, W. Xie, and R. J. Cava, APL Mater. **3,** 083602 (2015).
[46] Y.-H. Chan, C.-K. Chiu, M. Y. Chou, and A. P. Schnyder, Phys. Rev. B **93,** 205132 (2016).
[47] T. Bzdusek, Q. Wu, A. Ruegg, M. Sigrist, and A. A. Soluyanov, Nature **538,** 75 (2016).
[48] Z. Yan and Z. Wang, Phys. Rev. Lett. 117, 087402 (2016).
[49] C.-K. Chan, Y.-T. Oh, J. H. Han, and P. A. Lee, Phys. Rev. B **94,** 121106 (2016).
[50] G. Bian, T. R. Chang, R. Sankar R, S.-Y. Xu, H. Zheng, T. Neupert, C.-K. Chiu, S.-M. Huang, G. Chang, I. Belopolski, D. S. Sanchez, M. Neupane, N. Alidoust, C. Liu, B. Wang, H.-T. Jeng, A. Bansil, F. Chou, H. Lin, and M. Z. Hasan, Nat. Commun. **7,** 10556 (2016).
[51] C. L. Zhang, Z. J. Yuan, G. Bian, S. Y. Xu, X. Zhang, M. Z. Hasan, and S. Jia, Phys. Rev. B **93,** 054520 (2016).
[52] M. Ezawa, Phys. Rev. Lett. **116,** 127202 (2016).
[53] G. Kresse and J. Furthmüller, Phys. Rev. B **54,** 11169 (1996).
[54] R. Armiento and A. E. Mattsson, Phys. Rev. B **72,** 085108 (2005).
[55] P. E. Blöchl, Phys. Rev. B **50,** 17953 (1994).
[56] J. P. Perdew, K. Burke, and M. Ernzerhof, Phys. Rev. Lett. **77,** 3865 (1996).
[57] J. Heyd, G. E. Scuseria, and M. Ernzerhof, J. Chem. Phys. **124,** 219906 (2006).
[58] A. Togo, F. Oba, and I. Tanaka, Phys. Rev. B **78,** 134106 (2008).
[59] J. T. Wang, C. F. Chen, H. Mizuseki, and Y. Kawazoe, Phys. Rev. Lett. **110,** 165503 (2013).
[60] C. S. Lian and J. T. Wang, J. Chem. Phys. **140,** 204709 (2014).
[61] The polymeric (3,3) CNT can be formed spontaneously from (3,3) CNT based on an intertube sliding-assisted cross-linking mechanism under pressure [60]. The polymerization pathway is shown in Fig. S1 in Supplemental Material [62]. It contains two (3,3) CNTs in $Imma$ (D_{2h}^{28}) symmetry [see Fig. 1(b)]. The lattice parameters are a = 8.536 Å, b = 2.485 Å, and c = 9.025 Å, occupying the 8i (0.4216, 0.25. 0.2341), 8i (0.1979, 0.25, 0.5374), and 8i (0.1711, 0.25, 0.7057) Wyckoff positions. It is a semicondutor with a direct band gap of 0.32 eV at the R point of the Brillouin zone.
[62] See Supplemental Material for the initial stage pathway from (3,3) CNT toward polymeric (3,3) CNT (Fig. S1); the enthalpy changes versus pathway from polymeric (3,3) CNT toward bct-C_{12} and ign-C_6 at 10 GPa (Fig. S2); calculated surface band structures for the surface with the outermost atoms of C_1 (Fig. S3); band structures and Berry phase result (Fig. S4) based on a tight-binding model.
[63] W. I. F. David, R. M. Ibberson, J. C. Matthewman, K. Prassides, T. J. S. Dennis, J. P. Hare, H. W. Kroto, R. Taylor, and D. R. M. Walton, Nature **353,** 147 (1991).
[64] F. D. Murnaghan, Proc. Nat. Acad. Sci. U.S.A. **30,** 244 (1944).
[65] J. T. Wang, C. F. Chen, D. S. Wang, H. Mizuseki, and Y. Kawazoe, J. Appl. Phys. **107,** 063507 (2010).
[66] S. Nosé, J. Chem. Phys. **81,** 511 (1984).
[67] T. Hyart, R. Ojajarvi and T. T. Heikkila, J. Low Temp. Phys. *191,* 35 (2018).
[68] Q. Wu, S. Zhang, H.-F. Song, M. Troyer, and A. A. Soluyanov, arXiv:1703.07789.
[69] A. A. Mostofi, J. R. Yates, Y.-S. Lee, I. Souza, D. Vanderbilt, and N. Marzari, Comput. Phys. Commun. **178,** 685 (2008).